Libertas Academica
FREEDOM TO RESEARCH

Open Access: Full open access to this and thousands of other papers at http://www.la-press.com.

Magnetic Resonance Insights

Damage to the Optic Chiasm in Myelin Oligodendrocyte Glycoprotein–Experimental Autoimmune Encephalomyelitis Mice

Sheryl L. Herrera[1,*], Vanessa L. Palmer[2,*], Heather Whittaker[3], Blair Cardigan Smith[4], Annie Kim[5], Angela E. Schellenberg[5,6], Jonathan D. Thiessen[7,8], Richard Buist[9], Marc R. Del Bigio[10] and Melanie Martin[1,2,4,5,9]

[1]Physics and Astronomy, University of Manitoba, Winnipeg, Manitoba, Canada. [2]Biomedical Engineering Program, University of Manitoba, Winnipeg, Manitoba, Canada. [3]Biopsychology Program, University of Winnipeg, Winnipeg, Manitoba, Canada. [4]Physics, University of Winnipeg, Winnipeg, Manitoba, Canada. [5]Pharmacology and Therapeutics, University of Manitoba, Winnipeg, Manitoba, Canada. [6]General Surgery, University of Saskatchewan, Saskatoon, Saskatchewan, Canada. [7]Imaging Program, Lawson Health Research Institute, London, Ontario, Canada. [8]Medical Biophysics, Western University, London, Ontario, Canada. [9]Radiology, University of Manitoba, Winnipeg, Manitoba, Canada. [10]Pathology, University of Manitoba, Winnipeg, Manitoba, Canada. *These authors contributed equally to this work.

ABSTRACT: Optic chiasm lesions in myelin oligodendrocyte glycoprotein (MOG)–experimental autoimmune encephalomyelitis (EAE) mice were characterized using magnetic resonance imaging (MRI) and validated using electron microscopy (EM). MR images were collected from 3 days after induction to remission, approximately 20 days after induction. Hematoxylin and eosin, solochrome cyanin–stained sections, and EM images were obtained from the optic chiasms of some mice approximately 4 days after disease onset when their scores were thought to be the highest. T_2-weighted imaging and apparent diffusion coefficient map hyperintensities corresponded to abnormalities in the optic chiasms of EAE mice. Mixed inflammation was concentrated at the lateral surface. Degeneration of oligodendrocytes, myelin, and early axonal damage were also apparent. A marked increase in chiasm thickness was observed. T_2-weighted and diffusion-weighted MRI can detect abnormalities in the optic chiasms of MOG-EAE mice. MRI is an important method in the study of this model toward understanding optic neuritis.

KEYWORDS: experimental autoimmune encephalomyelitis, mouse, pertussis toxin, optic chiasm, magnetic resonance imaging

CITATION: Herrera et al. Damage to the Optic Chiasm in Myelin Oligodendrocyte Glycoprotein–Experimental Autoimmune Encephalomyelitis Mice. *Magnetic Resonance Insights* 2014:7 23–31 doi:10.4137/MRI.S19750.

RECEIVED: August 27, 2014. **RESUBMITTED:** September 30, 2014. **ACCEPTED FOR PUBLICATION:** October 2, 2014.

ACADEMIC EDITOR: Sendhil Velan, Editor in Chief

TYPE: Original Research

FUNDING: The authors thank funding support provided by Natural Sciences and Engineering Research Council of Canada. Dr Del Bigio holds the Canada Research Chair in Developmental Neuropathology. The authors confirm that the funder had no influence over the study design, content of the article, or selection of this journal.

COMPETING INTERESTS: Authors disclose no potential conflicts of interest.

CORRESPONDENCE: m.martin@uwinnipeg.ca

Paper subject to independent expert blind peer review by minimum of two reviewers. All editorial decisions made by independent academic editor. Upon submission manuscript was subject to anti-plagiarism scanning. Prior to publication all authors have given signed confirmation of agreement to article publication and compliance with all applicable ethical and legal requirements, including the accuracy of author and contributor information, disclosure of competing interests and funding sources, compliance with ethical requirements relating to human and animal study participants, and compliance with any copyright requirements of third parties. This journal is a member of the Committee on Publication Ethics (COPE).

Introduction

Multiple sclerosis (MS) is one of the most common chronic central nervous system (CNS) disorders affecting young adults.[1] Key pathological hallmarks of MS include myelin damage, inflammation, and neurodegeneration.[2] A number of animal models demonstrate the CNS pathology of MS. These include myelin mutants, chemical-induced lesions and viral models.[2–5] The most common model and extensively studied model of MS is experimental autoimmune encephalomyelitis (EAE).[6]

There are many similar characteristics between EAE and MS including genetic susceptibility, environmental triggers, white and gray matter pathology, clinical presentation, clinical forms, and clinical progression.[7] One way EAE can be induced in susceptible animals is through immunization with a number of myelin antigens, including myelin basic protein, proteolipid protein, and myelin oligodendrocyte glycoprotein (MOG).[5,8]

Optic neuritis has been considered a presenting symptom of, or a relapse in, MS.[9] People with MS frequently experience

optic neuritis at some time in their disease course, and 40%–70% of clinically isolated optic neuritis cases progress to MS.[10–12] Optic nerve lesions have been reported in some EAE models with certain cases developing optic neuritis.[13–18] These EAE models that develop optic neuritis could serve as a model for early detection of MS.

In one model, EAE was induced in inbred female NOD/Lt and C57Bl/6 with $MOG_{35–55}$ peptide. In this model, the degree of axonal pathology correlates with the intensity of inflammation and is more severe in the optic nerve than the spinal cord.[19,20] In another model, EAE was induced in SJL/J mice using proteolipid protein peptide 139–151. In this model, it was found that inflammatory cell infiltration mediates demyelination and leads to direct axonal injury.[21] In several mouse models, the same group found that inflammation precedes retinal ganglion cell loss and thus suggest that neuronal loss during optic neuritis occurs secondary to the inflammation process.[22,23] In another study, the same group found that different clinical disease courses of optic nerve inflammation might trigger distinct mechanisms of neuronal or retinal ganglion cell damage in different rodent strains.[24]

Another group focused on understanding the role of sodium channels in EAE. Using immunocytochemical methods to study the organization of sodium channels along axons in EAE-mice, a loss of $Nav_{1.6}$ and increased expression of $Nav_{1.2}$ was found suggesting that electrogenesis in EAE might revert to a stage similar to that observed in immature retinal ganglion cells in which $Nav_{1.2}$ channels support conduction of action potentials along axons.[25] Altered expression of these two distinct isoforms of sodium channels underlies two processes leading to the recovery of ability or disability of demyelinating axons to conduct impulses despite the absence of myelin.[26]

In order for a more complete understanding of axonal pathology, inflammation, demyelination, retinal ganglion cell loss, and the role of sodium channels along axons in optic neuritis models, it is important to develop in vivo methods to monitor and study optic neuritis as an early biomarker for MS and EAE. Magnetic resonance imaging (MRI) is an increasingly important method for the monitoring of MS and EAE.[27,28] Optic neuritis has been imaged using MRI in an EAE model in a marmoset monkey[27,29] and in mice using contrast agents.[27,30,31] These methods were highly sensitive to the detection of optic nerve lesions as early indicators of clinical disease formation.[30,31] The MRI techniques developed through such research on animal models have clear clinical translations, but they employ the contrast agent gadofluorine-M, which is not approved for use in human patients.[27]

MRI has been used to study the effect of treatments for optic neuritis animal models.[32] The disruption of the blood-brain barrier (BBB) and demyelination in an EAE optic neuritis guinea pig model was studied using T_2-weighted and Gd-diethylenetriaminepentacetate (DTPA)–enhanced T_1-weighted MRI.[33] Changes in MR images corresponded with optic nerve abnormalities and were lessened with catalase detoxification of endogenous H_2O_2 in these mice.[33] Optic neuritis mouse models were also studied by the same group using MRI as one of many in vivo monitoring tools.[34,35] MOG+ mice with the poorest vision assessed using pattern electroetinograms were shown to have optic nerve atrophy using MRI.[34] MRI measurements of the optic nerve showed it was not atrophic in mice with the human extracellular superoxide dismutase or catalase gene cloned into recombinant adeno-associated virus.[35] A review of animal studies using MRI to assess optic nerve damage indicates diffusion metrics are valuable in the assessment of optic nerve damage.[36]

Here we studied an EAE model that develops optic nerve lesions[36–38] as a means to characterize these lesions and to determine the efficacy of MRI without using contrast agents for the detection of the lesions.

In our model, we administered MOG along with pertussis toxin in order to facilitate entry of the antigen to the CNS across the BBB.[37–39] A previous study has shown BBB disruption in transgenic mice injected with pertussis toxin.[40] The authors concluded that the integrity of the BBB could be disrupted by pertussis toxin only if the necessary genetic and environmental stimuli were present. To determine if pertussis toxin has any independent role in optic nerve lesions, we have also examined a small group of mice, called pertussis toxin sham mice, which we injected only with the pertussis toxin, and not with MOG or complete Freund's adjuvant (CFA).

Materials and Methods

EAE mice. Forty-two 11-week-old C57Bl/6 mice (Genetic Models Centre [GM], Winnipeg, Canada [n = 34] and Charles River [CR], Canada [n = 8]) were classified into three groups: MOG-EAE (n = 30 [25 GM, 5 CR]), pertussis toxin sham (n = 3 [2 GM, 1 CR]), and control (n = 9 [7 GM, 2 CR]). As with previous studies, MOG-EAE mice received 50 µg of $MOG_{35–55}$ (The University of Calgary's Peptide Facility; 0.5 mg/mL in phosphate-buffered saline) mixed 1:1 with CFA (Fisher) in two 50-µL subcutaneous injections near the tail[37–39] on day 0. Also on day 0 and again on day 2, the MOG-EAE mice and the pertussis toxin sham mice received an intraperitoneal injection of 0.3 µg of pertussis toxin in 200 µL of phosphate-buffered saline.[37,41] Twenty-two other C57Bl/6 mice received MOG, pertussis toxin, and CFA but did not develop signs of EAE and were therefore excluded from the study.

Mice were housed in separate cages in the University of Manitoba animal facility with a 12-h dark/12-h light cycle, fed standard chow ab libitum, and monitored for up to 29 days after immunization. Mice were assessed daily starting on day 3 and given a score using a previously validated 0- to 5-point scoring system and a 0- to 14-point scoring system.[39,42] All mice underwent MR imaging, as described below, before their scores deviated from 0, termed predisease,

and when scores first deviated from 0, termed onset. Some mice (n = 7 [2 GM, 5 CR]) were imaged through remission every time their score changed by at least 2 on the 14-point scale but no more often than every other day. Another set of mice (n = 23 [23 GM]) was only imaged once more approximately 4 days after onset when their scores were felt likely to be the highest. These mice were sacrificed after imaging that day. Control mice and sham mice were imaged on the same days as the EAE mice.

The experimental protocol was approved by local institutional animal care committees who adhere to the guidelines and principles created by the Canadian Council on Animal Care.

Magnetic resonance imaging. T_2-weighted and diffusion-weighted MR images were collected from all mice at each imaging session using a 7 T/21 cm Bruker Biospec 3 spectrometer running Paravision 2.0.1 with a 2-cm inner diameter (I.D.) send/receive quadrature radiofrequency (RF) coil. Mice were anesthetized using 5% isoflurane in O_2/N_2O and maintained at 1.5%–2% isoflurane in O_2/N_2O with a nose cone. Respiration and external body temperature were monitored during imaging using an MR-compatible small animal monitoring and gating system (SA Instruments, Inc.). External body temperature was maintained at 37°C by adding cool or warm air when necessary.

T_2-weighted images were collected from each animal using a 0.75-mm slice with 2.5 × 2.5-cm^2 field of view and 98 μm in plane resolution using a multiecho (8 echos) T_2-weighted sequence. Each set of images was acquired in 21 minutes with a repetition time (TR) of 2500 ms and echo spacing of 27 ms and two averages.

Diffusion-weighted images (DWIs) were also collected from each animal using a slice thickness of 1 mm, field of view of 4 × 4 cm^2 and in-plane resolution of 313 μm, and a magnetization-prepared Turbo-FLASH (fast low-angle shot) sequence.[43,44] Three sets of images were acquired, each of which with diffusion weighting in one of three directions (x, y, and z). Eight b-values were acquired in each direction, namely b = 21 s/mm^2, b = 1031 s/mm^2, b = 189 s/mm^2, 336 s/mm^2, 757 s/mm^2, 84 s/mm^2, 1346 s/mm^2, and 525 s/mm^2, all with gradient pulse length δ = 18 ms and gradient separation Δ = 20 ms. The b-values were calculated using the diffusion-weighting factor equation for symmetric and square gradient pulses, $b = \gamma^2 g^2 \delta^2 (\Delta - \delta/3)$.[45] To correct for distortions due to phase shift, the quadratic summation of two complementary images at each b-value was used, with the second image having a 90° flip-back pulse phase shifted by $\pi/2$ with respect to the first.[43,44] Scan time was 16 min and 20 s for each set of DWIs, for a total DWI scan time of 3 × 2 × 16 min or 1 h 38 min.

MRI analysis. Using a custom-built MATLAB GUI, images with diffusion weighting in each direction were calculated using the square root of the sum of the square of each complimentary image. Apparent diffusion coefficient (ADC) maps in each of the three directions were calculated by fitting the natural log of the signal versus b-value on a voxel-by-voxel basis using the eight b-value images per direction. Mean ADC maps, which are presented here, were created by summing the three ADC directional maps and dividing by 3.

Regions of interest (ROIs) containing the third ventricle and a hyperintense region in the optic chiasm area were defined in all images of EAE mice at onset and near-peak stages of the disease. The optic chiasm was defined only on the right side of the image for simplicity. For control mice and EAE mice at predisease, the ROI for the optic chiasm was drawn in the same area where the hyperintensities appeared in the EAE images. An example is shown in Figure 1. The ratio of the mean ADC in the ROI from the optic chiasm area to the mean ADC in the third ventricle was calculated for each mouse and termed the relative ADC. The mean and standard deviation of relative ADC values and relative T_2-weighted signal intensities for all mice at each stage (control, predisease, onset, and near-peak disease) were calculated.

Statistics. To determine whether there were statistically significant effects in the disease stage with the relative ADC values and relative T_2-weighted signal intensities, statistics were performed using SAS® 9.3 software. One-way analysis of variance (ANOVA) was used to measure the significance in the effects of relative ADC values and relative T_2-weighted signal intensities based on the disease stage (predisease, onset, near peak, and control). If any significant differences between the stages existed, then a post hoc test (Duncan's multiple range) was used to test for significance. Statistical significance was determined using a threshold value of 0.05, where any P-values less than 0.05 would indicate a statistically significant difference.

Histology and electron microscopy. Immediately after imaging, mice were anesthetized with 1.5%–2% isoflurane and perfused through the heart with fixative. In a pilot study (n = 4) we used phosphate-buffered 10% formalin followed by dehydration and embedding in paraffin wax. Six-micrometer coronal slices stained with Harris hematoxylin and eosin (HE) and solochrome cyanin (SC) showed loss of myelin staining and inflammation, but insufficient detail for interpretation of the MR images. The remaining mice (n = 38) were fixed with 2% glutaraldehyde in phosphate-buffered saline. Brains were removed from the skull and stored overnight at 4°C in the same fixative. The optic chiasm was isolated, split in the midline ensuring the left–right orientation was not lost, postfixed in 1% osmium tetroxide, dehydrated through graded alcohols, and embedded in epoxy resin. Semithin sections (0.5 μm) were stained with toluidine blue. Thin sections (80 nm) were mounted on copper grids and contrasted with uranyl acetate–lead citrate for electron microscopic (EM) examination (JEOL 1010 microscope) by an observer (MRD) blinded to the nature of the intervention.

Results

Mean weights and scores were calculated daily starting at day 3 after induction and going to remission for the EAE

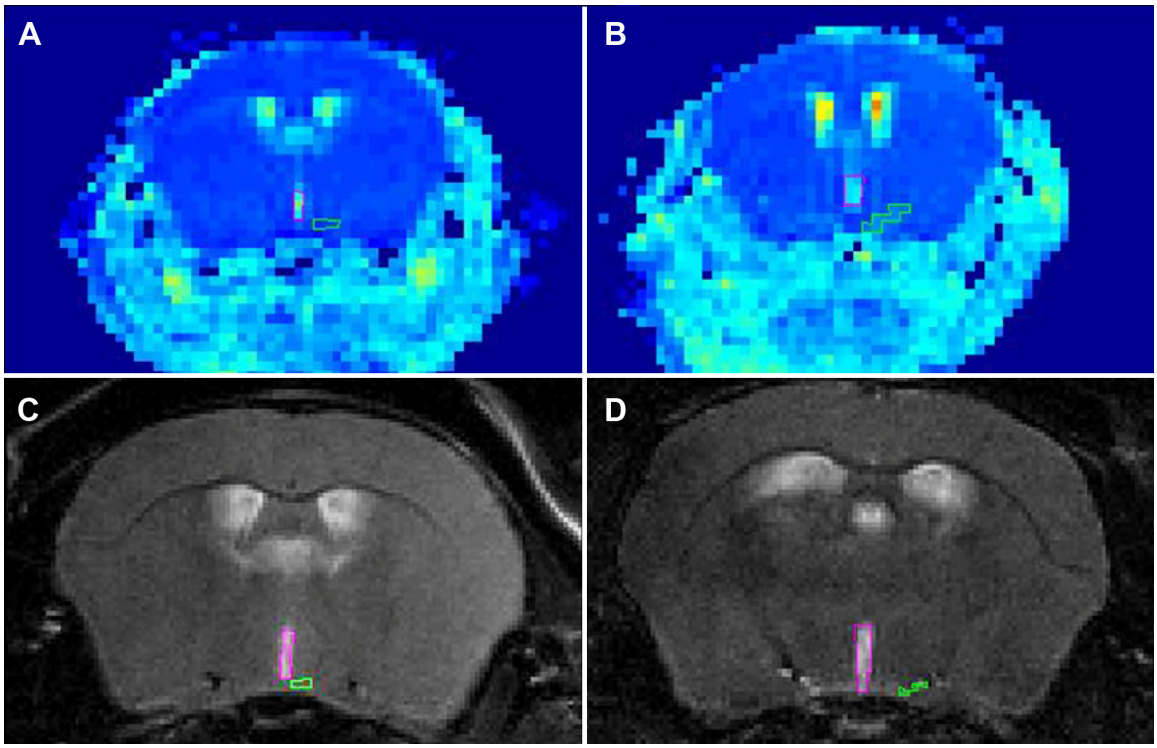

Figure 1. ROIs used to compare hyperintensities. Example ADC maps (**A** and **B**) and T_2-weighted images (**C** and **D**) of control mice (**A** and **C**) and EAE mice whose scores were near-peak (**B** and **D**) are shown with the ROIs used to define the third ventricle (magenta) and the optic chiasm (green).

mice that were not sacrificed for ex vivo tissue analysis ($n = 7$, 2 GM, 5 CR). The results are shown in Figure 2. Consistent with other studies, the mouse weight was lowest when the scores were highest.[39,42] Similar to these other studies, onset of the disease occurred between day 9 and 15 after induction, peak disease occurred between day 12 and 19, and remission occurred between day 18 and day 26.[37–39,41]

R^2 for the fits to the data to calculate the ADC maps in the voxels in the ROI of the optic chiasm indicated that a mono-exponential fit to the data was appropriate.

Both mean ADC maps (Fig. 3A) and T_2-weighted images (Fig. 3B) showed hyperintensities around the optic chiasm of EAE mice with nonzero scores when compared to control and pertussis toxin sham mice. The red boxes in Figure 3 correspond to the areas featured in Figure 4 where larger images of the area containing and surrounding the optic chiasm for three controls and three EAE mice show these hyperintensities in more detail.

The mean and standard deviation of relative ADC values and relative T_2-weighted signal intensities for all mice, both control and EAE at each stage (predisease, onset, and near-peak disease), are summarized in Table 1.

One-way ANOVA was conducted on the disease stages (control and three EAE stages) and showed no statistical non-significance between the relative ADC values [$F(3,74) = 1.84$, $P = 0.1472$].

One-way ANOVA also showed that the overall effect of disease stage (control and three EAE stages) on relative T_2-weighted signal intensities was statistically different [$F(3,56) = 11.32$, $P < 0.0001$]. To verify this, Duncan's multiple range post hoc test also confirmed the statistical differences (P-values < 0.05) between the following stages: predisease between both near-peak and control; and onset between near-peak and control. All other comparisons between the disease stages were not statistically significantly different.

Light and EM examination showed abnormalities corresponding with the locations of MRI hyperintensities. The optic chiasms from the mice that developed experimental optic neuritis had intense inflammatory infiltrates on the surface especially around the blood vessels from day 14–17 (Fig. 5A). At the light microscopic level, the optic chiasms of control mice consisted of densely packed, myelinated axons with thin-walled blood vessels on the ventral surface (Fig. 5B). Morphologically, the inflammatory cells included lymphocytes and neutrophils. Some inflammatory cells were identifiable within the chiasm, and the myelinated axons appeared dispersed, possibly because of edema.

Ultrastructural examination of the optic chiasms from control mice showed veins on the ventral surface and myelin sheaths surrounding all but the smallest axons (Fig. 6A). No inflammatory cells could be identified. The optic chiasms from mice with experimental optic neuritis showed a mixed inflammatory cell population concentrated at the lateral surface and surrounding the superficial blood vessels (Fig. 6B). The cells had morphologic features characteristic of lymphocytes and neutrophils. A few inflammatory cells invaded the

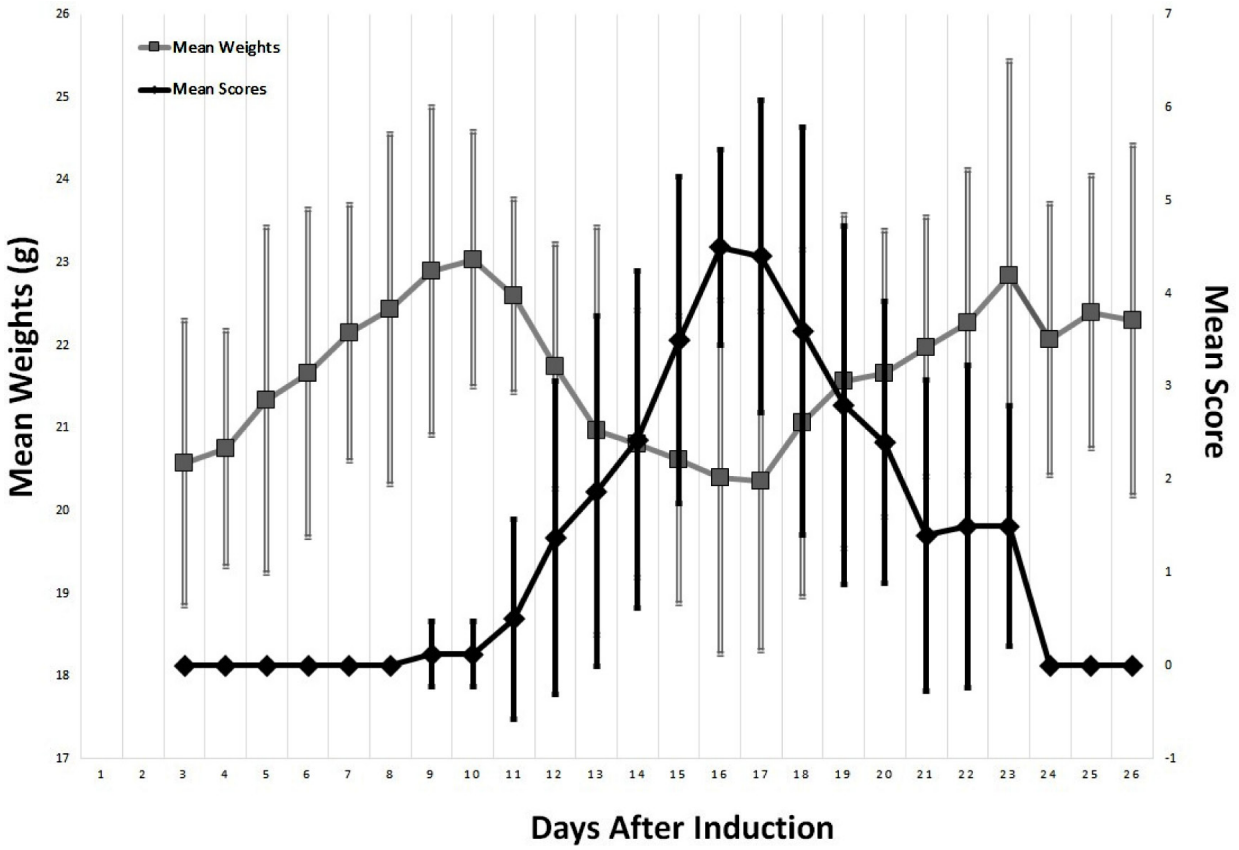

Figure 2. Mouse weights and scores during EAE disease course. Average ± standard deviation of mouse weights and scores are plotted versus day after EAE induction. Mouse weights dropped when their scores peaked. Seven mice were studied from onset (day 9–15) through peak disease (day 12–19) and remission (day 18–26). Another subset of 23 mice were used for histology and EM around near-peak disease and thus were not included in this graph.

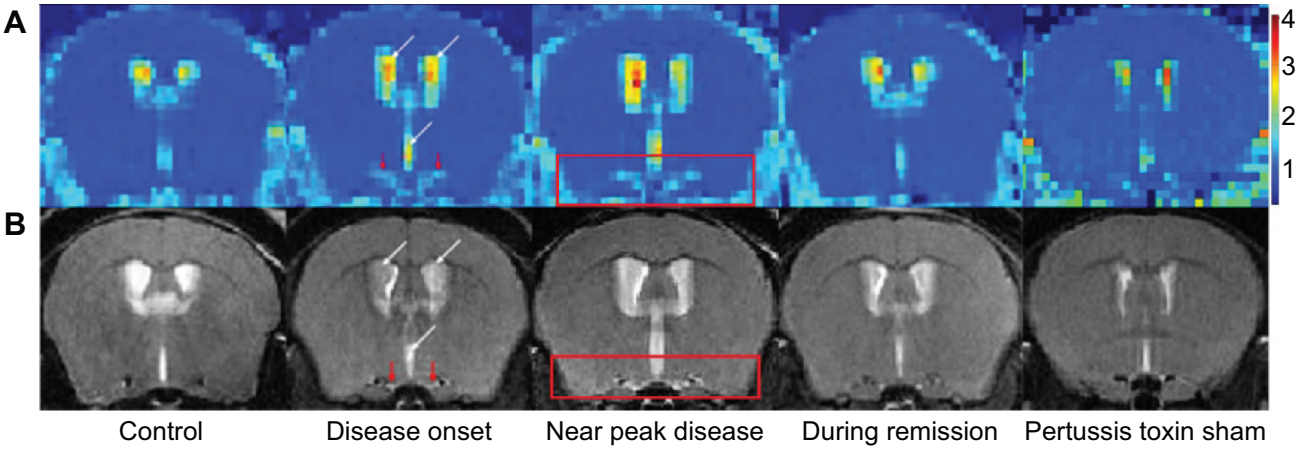

Figure 3. Hyperintensities around and in the optic chiasm are seen in mean ADC maps (**A**) and T_2-weighted (**B**) MR images of EAE mice and not in most control mice or pertussis toxin sham mice. Hyperintensities near the optic chiasm (red arrows) are seen in mean ADC maps (**A**) and T_2-weighted images (TE = 54 ms) (**B**) in EAE mice at disease onset and at near-peak disease when a higher disease score thought to be peak disease was observed. Disease onset occurred between day 9 and 15 after induction, peak disease occurred between day 12 and 19, and remission occurred between day 18 and day 26. The most hyperintense regions in all images include the lateral ventricles and the third ventricle as shown with the white arrows and are not due to EAE. No abnormal hyperintensities are seen in either type of image in the pertussis toxin sham mice, most control mice or during remission in the EAE mice. Voxel size in the T_2-weighted images is $98 \times 98 \times 750$ μm^3. Voxel size in the ADC maps is $313 \times 313 \times 1000$ μm^3. The scale bar on the right, which explains the color intensities, corresponds to all ADC maps with units of 10^{-3} mm^2/s.

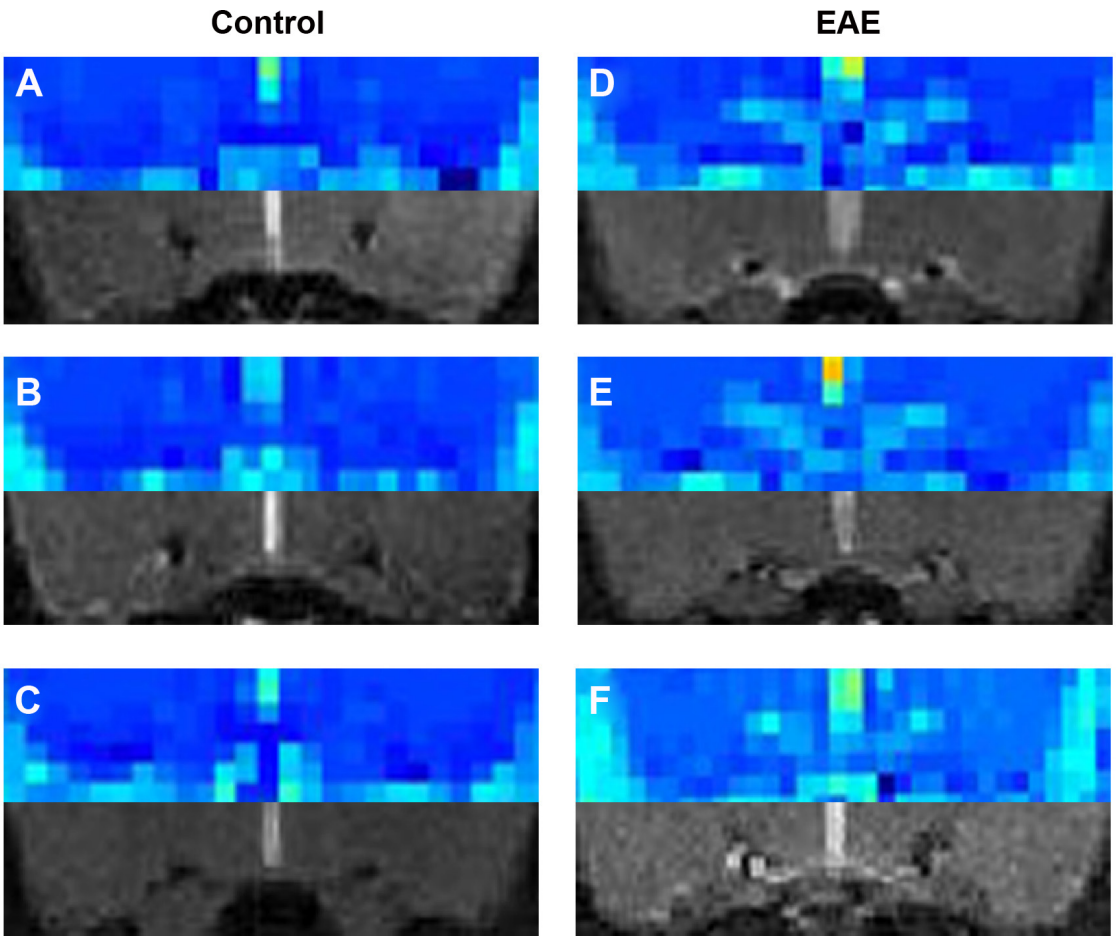

Figure 4. ADC maps (top, color) and T_2-weighted images (bottom, black and white) for three control mice (**A**–**C**) and three EAE mice near-peak disease (**D**–**F**) of the optic chiasm area (from regions corresponding to the red box in Fig. 2) are shown to highlight the hyperintensities. The same scale bar from Figure 2 applies to these images.

chiasms and were associated with hypertrophic (activated) microglia. Degeneration of oligodendrocytes, myelin, and early axonal damage were also apparent (Fig. 6C). Possibly because of the combination of abnormalities (inflammatory cell invasion, delamination of myelin, axon and cell swelling, and an increase in extracellular volume) a marked increase in chiasm thickness was observed.

Although the MR images of the pertussis toxin sham mice showed no abnormalities, EM examination showed minimal myelin sheath vacuolation and scattered axons with dispersed axoskeleton (Fig. 6D). The chiasm surface was slightly hypercellular, but the nature of the additional cells was not obvious.

Discussion

The MOG-EAE mouse model used in this study was demonstrated to be a suitable model for optic neuritis with MS. Lesions of the optic chiasm were clearly visible with MRI and presented as hyperintensities in most ADC maps and T_2-weighted images of EAE mice at onset and near-peak disease. Images classified as near-peak were collected when the score of the mouse was considered to be the highest, which was typically 4 days after onset. For a small number of mice, imaging had to be delayed up to 11 days after onset because of scanner availability. At that point, the mice were in remission and their scores had almost returned to 0. The only images labeled near-peak that did not show hyperintensities

Table 1. Relative metric values at different disease stages.

	CONTROL	PREDISEASE	ONSET	NEAR-PEAK
Relative ADC	0.7 ± 0.2	0.6 ± 0.2	0.7 ± 0.2	0.8 ± 0.2
Relative T_2-weighted signal intensity	0.5 ± 0.1*	0.8 ± 0.1*,†	0.8 ± 0.2*,†	0.6 ± 0.1†

Note: Statistical differences were found between the groups as indicated by * and †.

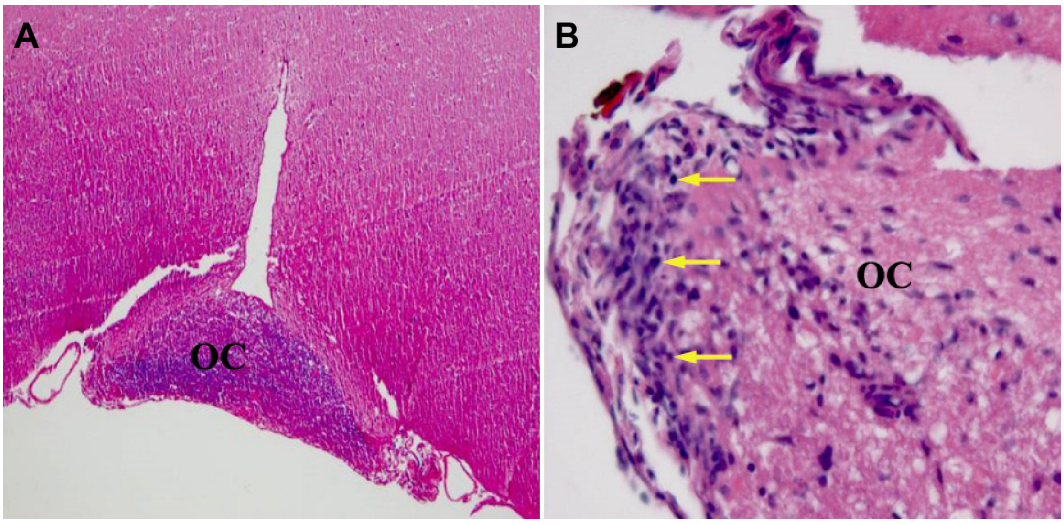

Figure 5. Inflammatory aggregates and suspected myelin reduction are visualized in the lateral regions of and within the optic chiasm of EAE mice. The pathological changes with EAE progression were examined with SC (**A**) and with HE (**B**). Inflammatory aggregates (arrows) and slight reduction of myelin staining (blue) are observed around the lateral regions and within the optic chiasm (OC). Photographs were taken at 40× (**A**) and 200× (**B**) magnification.

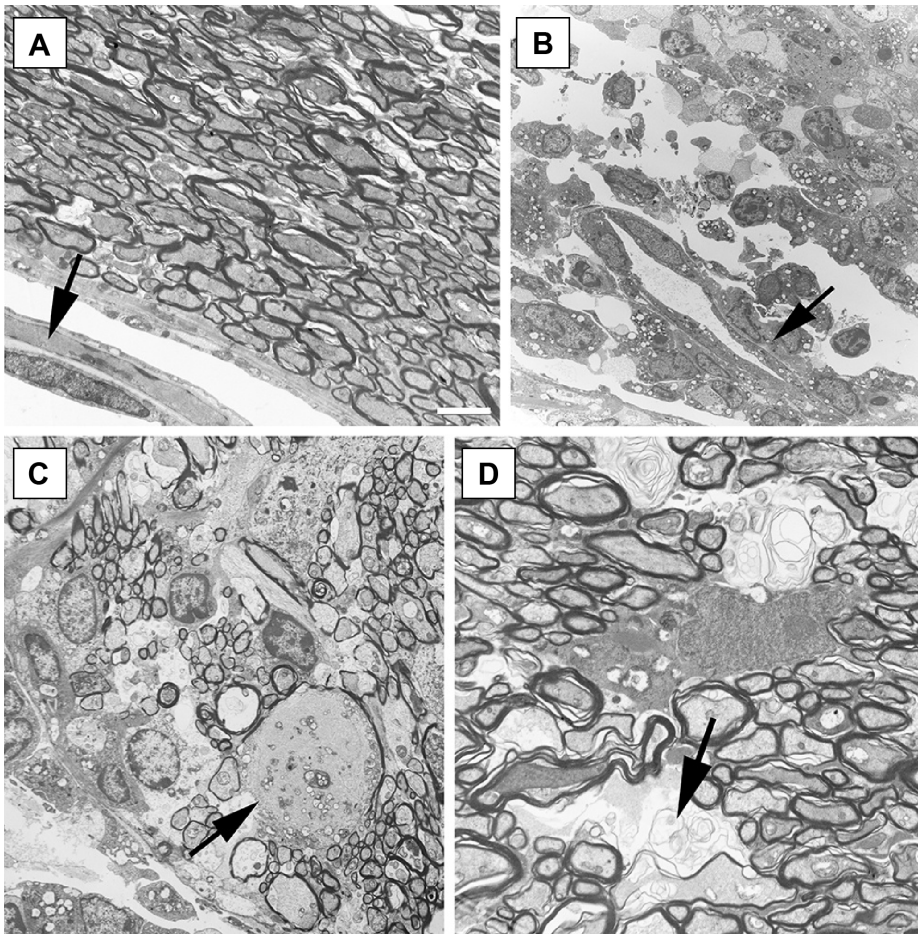

Figure 6. EM reveals pathological features in the optic chiasm associated with EAE. In wild-type control mice (**A**) associated veins (arrow) are visible on the surface. The myelin sheaths surrounded all but the smallest axons. EAE is associated with intense perivascular inflammation on the chiasm surface surrounding the blood vessels (arrow B). Lymphocytes and neutrophils invaded the chiasm. Damaged axons are swollen and partially denuded of myelin (arrow C). Pertussis toxin inoculations (sham controls) are associated with some myelin sheath vacuolations (arrow d). Bar = 2 μm (**A**). Photographs are taken at 8000× (**A**, **D**), 4000× (**B**), and 6000× (**C**) magnification.

were from mice that were imaged in remission, 9–11 days after onset. The hyperintense regions were of smaller area in the images of control mice and EAE mice at predisease than those in at-onset and near-peak.

Even though large hyperintense regions were visible in the ADC maps of EAE mice at onset and near-peak EAE, there were no significant differences between relative ADC values in the optic chiasms of any of the stages (control and three EAE stages) of disease. This could be due to artifacts in the images due to motion and the different angles at which the slices were collected skewing the ventricle intensities.

T_2-weighted images often were collected at different angles and contained different amounts of the third ventricle in each voxel. Thus, ratios between T_2-weighted signal intensities and ventricle intensities were sometimes skewed. Hyperintensities were visible in almost all the T_2-weighted images from EAE mice at onset and near-peak disease. As with the ADC maps, those at near-peak disease that did not show hyperintensities were collected during remission and not during peak.

Hyperintensities in T_2-weighted images and mean ADC maps are thought to correspond to abnormalities such as inflammation,[46–48] edema[49,50] and demyelination.[47,49,51] EM further revealed various signs of mixed inflammation concentrated at the lateral surface of the optic chiasm, intense perivascular inflammation on the chiasm surface that surrounds the blood vessels and to a lesser degree lymphocytes, and that neutrophils and microglia invaded the chiasms.

Similar EAE pathologies to those observed in this model were also observed in other studies of the optic nerves[19,20,52,53] and the optic chiasms of other EAE models.[54–57] In all these studies, inflammation was typically concentrated in and around the subarachnoid blood vessels of the optic nerve and chiasm. The effects of EAE on axons in the optic chiasm were milder in our study than these other studies. Our study further characterizes the optic lesions. The pertussis toxin sham mice developed mild myelin sheath vacuolation and enlarged axons, which, to our knowledge, has never been described. Previous studies reported no breakdown of the BBB or the blood–spinal cord barrier,[39,58] and no clinical and/or histological occurrences of optic neuritis or EAE from pertussis injections.[18]

This MOG-EAE mouse model could be used to understand better the role of optic neuritis in MS. The effective visualization of optic nerve lesions without the use of contrast agents is an important step in developing more powerful diagnostic tools for early stages of MS. More detailed MRI studies using multiple metrics such as those from T_2-weighted imaging, magnetization transfer imaging, and diffusion tensor imaging could provide more insight into the progression of pathological features in this mouse model.[59] With the used of larger *b*-values, Intravoxel Incoherent Motions (IVIM)-analysis would allow a study of the possible effects of perfusion on the diffusion data.[60] With a more thorough understanding of MS etiology that this model can provide, it could eventually be useful for testing innovative measures of controlling or halting the disease course. In addition to MRI, functional evaluation of vision, as has been previously performed on myelin-disrupted mice[61–63] would further be useful to characterize lesions and correlate their types and presence with functional disabilities.

Conclusion

Optic lesions were detected without contrast agents using T_2-weighted and diffusion-weighted MRI in an MOG-EAE mouse model. The hyperintensities in MRI corresponded with axonal pathology identified in EM and indicated the development of optic neuritis. Therefore, this model serves as an important tool for understanding optic neuritis associated with the onset of MS. MRI can be used reliably to monitor lesions in longitudinal studies, which might aid in the understanding of the pathological time course of lesions that characterize both optic neuritis and MS.

Author Contributions

Conceived and designed the experiments: BCS, AK, AES, RB, MRD, MM. Analyzed the data: SLH, VLP, BCS, AK, JDT, RB, MRD, MM. Wrote the first draft of the manuscript: SLH, VLP, HW, MM. Contributed to the writing of the manuscript: SLH, VLP, HW, AES, JDT, RB, MRD, MM. Agree with manuscript results and conclusions: SLH, VLP, HW, BCS, AK, AES, JDT, RB, MRD, MM. Jointly developed the structure and arguments for the paper: SLH, VLP, JDT, RB, MRD, MM. Made critical revisions and approved final version: SLH, VLP, HW, BCS, AK, AES, JDT, RB, MRD, MM. All authors reviewed and approved of the final manuscript.

REFERENCES

1. Multiple Sclerosis International Federation. Atlas of MS Database 2013; 2013. Available at http://www.msif.org/includes/documents/cm_docs/2013/m/msif-atlas-of-ms-2013-report.pdf?f=1. Accessed October 2, 2013.
2. Baker D, Gerritsen W, Rundle J, Amor S. Critical appraisal of animal models of multiple sclerosis. *Mult Scler J*. 2011;17(6):647–657.
3. Baker D, Jackson SJ. Models of multiple sclerosis. *Adv Clin Neurosci Rehabil*. 2007;6:10–12.
4. Fazakerley JK, Walker R. Virus demyelination. *J Neurovirol*. 2003;29:148–164.
5. Steinman L, Zambil SS. How to successfully apply animal studies in experimental allergic encephalomyelitis to research on multiple sclerosis. *Ann Neurol*. 2006;60:12–21.
6. Rivers TM, Schwentker FF. Encephalomyelitis accompanied by myelin destruction experimentally produced in monkeys. *J Exp Med*. 1935;61(5):689–702.
7. Steinman L. Optic neuritis, a new variant of experimental encephalomyelitis, a durable model for all seasons, now in its seventieth year. *J Exp Med*. 2003;197:1065–1071.
8. Bettelli E. Building different mouse models for human MS. *Ann N Y Acad Sci*. 2007;1103:11–18.
9. Petzold A, Plant GT. Chronic relapsing inflammatory optic neuropathy: a systematic review of 122 cases reported. *J Neurol*. 2014;261(1):17–26.
10. Soderstrom M. Optic neuritis and multiple sclerosis. *Acta Ophthalmol Scand*. 2001;79:223–227.
11. Ghezzi A, Martinelli V, Torri V, et al. Long-term follow-up of isolated optic neuritis: the risk of developing multiple sclerosis, its outcome, and the prognostic role of paraclinical tests. *J Neurol*. 1999;246:770–775.
12. Acheson J. Optic nerve and chiasmal disease. *J Neurol*. 2000;247:587–596.
13. Raine CS, Traugott U, Nussenblatt RB, Stone SH. Optic neuritis and chronic relapsing experimental allergic encephalomyelitis: relationship to clinical course and comparison with multiple sclerosis. *Lab Invest*. 1980;42:327–335.

14. Hayreh SS, Massanari RM, Yamada T, Hayreh SM. Experimental allergic encephalomyelitis. I. Optic nerve and central nervous system manifestations. *Invest Ophthalmol Vis Sci*. 1981;21(2):256–269.
15. Hayreh SS. Experimental allergic encephalomyelitis. II. Retinal and other ocular manifestations. *Invest Ophthalmol Vis Sci*. 1981;21:270–281.
16. O'Neill JK, Baker D, Morris MM, et al. Optic neuritis in chronic relapsing experimental allergic encephalomyelitis in Biozzi ABH mice: demyelination and fast axonal transport changes in disease. *J Neuroimmunol*. 1998;82:210–218.
17. Hu P, Pollard J, Hunt N, Taylor J, Chan-Ling T. Microvascular and cellular responses in the optic nerve of rats with acute experimental allergic encephalomyelitis (EAE). *Brain Pathol*. 1998;8:475–486.
18. Bettelli E, Pagany M, Weiner HL, Linington C, Sobel RA, Kuchroo VK. Myelin oligodendrocyte glycoprotein-specific T cell receptor transgenic mice develop spontaneous autoimmune optic neuritis. *J Exp Med*. 2003;197(9):1073–1081.
19. Wang D, Ayers MM, Catmull DV, Hazelwood LJ, Bernard CC, Orian JM. Astrocyte-associated axonal damage in pre-onset stages of experimental autoimmune encephalomyelitis. *Glia*. 2005;51:235–240.
20. Ayers M, Hazelwood L, Catmull D, et al. Early glial responses in murine models of multiple sclerosis. *Neurochem Int*. 2004;45:409–419.
21. Shindler KS, Ventura E, Dutt M, Rostami AM. Inflammatory demyelination induces axonal injury and retinal ganglion cell apoptosis in experimental optic neuritis. *Exp Eye Res*. 2008;87:208–213.
22. Shindler KS, Guan Y, Ventura E, Bennett J, Rostami AM. Retinal ganglion cell loss induced by acute optic neuritis in a relapsing model of multiple sclerosis. *Mult Scler*. 2006;12:526–532.
23. Guan Y, Shindler KS, Tabuena P, Rostami AM. Retinal ganglion cell damage induced by spontaneous autoimmune optic neuritis in MOG-specific TCR transgenic mice. *J Neuroimmunol*. 2006;178:40–48.
24. Quinn TA, Dutt M, Shindler KS. Optic neuritis and retinal ganglion cell los in a chronic murine model of multiple sclerosis. *Front Neurol*. 2011;2:50.
25. Craner MJ, Lo AC, Black JA, Waxman SG. Abnormal sodium channel distribution in optic nerve axons in a model of inflammatory demyelination. *Brain*. 2003;126:1552–1561.
26. Waxman SG, Craner MJ, Black JA. Na+ channel expression along axons in multiple sclerosis and its models. *Trends Pharmacol Sci*. 2004;25(11):584–591.
27. Nathoo N, Wee Yong V, Dunn JF. Understanding disease processes in multiple sclerosis through magnetic resonance imaging studies in animal models. *Neuroimage Clin*. 2014;4:743–756.
28. Filippi M, Rocca MA. MR imaging of multiple sclerosis. *Radiology*. 2011;259(3): 659–681.
29. Boretius S, Schmelting B, Watanabe T, et al. Monitoring of EAE onset and progression in the common marmoset monkey by sequential high-resolution 3D MRI. *NMR Biomed*. 2006;19(1):41–49.
30. Wuerfel E, Infante-Duarte C, Glumm R, Wuerfel JT. Gadofluorine M-enhanced MRI shows involvement of circumventricular organs in neuroinflammation. *J Neuroinflammation*. 2010;7:70.
31. Wuerfel J, Tysiak E, Prozorovski T, et al. Mouse model mimics multiple sclerosis in the clinico-radiological paradox. *Eur J Neurosci*. 2007;26(1):190–198.
32. Guy J. MRI in experimental inflammatory and mitochondrial optic neuropathies. *NMR Biomed*. 2008;21:968–977.
33. Guy J, McGorray S, Fitzsimmons J, et al. Reversals of blood-brain barrier disruption by catalase: a serial magnetic resonance imaging study of experimental optic neuritis. *Invest Ophthalmol Vis Sci*. 1994;35(9):3456–3465.
34. Talla V, Yang C, Shaw G, Porciatti V, Koilkonda RD, Guy J. Noninvasive assessments of optic nerve neurodegeneration in transgenic mice with isolated optic neuritis. *Invest Ophthalmol Vis Sci*. 2013;54:4440–4450.
35. Qi X, Sun L, Lewin AS, Hauswirth WW, Guy J. Long-term suppression of neurodegeneration in chronic experimental optic neuritis: antioxidant gene therapy. *Invest Ophthalmol Vis Sci*. 2007;48:5360–5370.
36. Xu J, Sun S-W, Naismith RT, Snyder AZ, Cross AH, Song S-K. Assessing optic nerve pathology with diffusion MRI: from mouse to human. *NMR Biomed*. 2008;21:928–940.
37. Tsutsui S, Schnermann J, Noorbakhsh F, et al. A1 adenosine receptor upregulation and activation attenuates neuroinflammation and demyelination in a model of multiple sclerosis. *J Neurosci*. 2004;24:1521–1529.
38. Giuliani F, Fu SA, Metz LM, Yong VW. Effective combination of minocycline and interferon-beta in a model of multiple sclerosis. *J Neuroimmunol*. 2005; 165:83–91.
39. Schellenberg AE, Buist R, Wee Yong V, Del Bigio MR, Peeling J. Magnetic resonance imaging of blood–spinal cord barrier disruption in mice with experimental autoimmune encephalomyelitis. *Magn Reson Med*. 2007;58:298–305.
40. Schellenberg AE, Buist R, Del Bigio MR, et al. Blood–brain barrier disruption in CCL2 transgenic mice during pertussis toxin-induced brain inflammation. *Fluids Barriers CNS*. 2012;9:10.
41. Oliver AR, Lyon GM, Ruddle NH. Rat and human myelin oligodendrocyte glycoproteins induce experimental autoimmune encephalomyelitis by different mechanisms in C57/BL16 mice. *J Immunol*. 2003;171(1):462–468.
42. Giuliani F, Metz LM, Wilson T, Fan Y, Bar-Or A, Wee Yong V. Additive effect of the combination of glatiramer acetate and minocycline in a model of MS. *J Neuroimmunol*. 2005;158(1):213–221.
43. Thomas DL, Pell GS, Lythgoe MF, Gadian DG, Ordidge RJ. A quantitative method for fast diffusion imaging using magnetization-prepared TurboFLASH. *Magn Reson Med*. 1998;39:950–960.
44. Thiessen JD, Glazner KAC, Nafez S, et al. Histochemical visualization and diffusion MRI at 7 Tesla in the TgCRND8 transgenic model of Alzheimer's disease. *Brain Struct Funct*. 2010;215:29–36.
45. Stejskal E, Tanner J. Spin diffusion measurements: spin echoes in the presence of a time-dependent field gradient. *J Chem Phys*. 1965;42:288–292.
46. McDonald WI, Barnes D. Lessons from magnetic resonance imaging in multiple sclerosis. *Trends Neurosci*. 1989;12:376–379.
47. McDonald WI, Miller DH, Barnes D. The pathological evolution of multiple sclerosis. *Neuropathol Appl Neurobiol*. 1992;18:319–334.
48. Nessler S, Boretius S, Stadelmann C, et al. Early MRI changes in a mouse model of multiple sclerosis are predictive of severe inflammatory tissue damage. *Brain*. 2007;130(8):2186–2198.
49. Bruck W, Bitsch A, Kolenda H, Bruck Y, Stiefel M, Lassmann H. Inflammatory central nervous system demyelination: correlation of magnetic resonance imaging findings with lesion pathology. *Ann Neurol*. 1997;42:783–793.
50. Ebisu T, Naruse S, Horikawa Y, et al. Discrimination between different types of white matter edema with diffusion-weighted MR imaging. *J Magn Reson Imaging*. 1993;3:863–868.
51. van Waesberghe JH, Kamphorst W, DeGroot CJ, et al. Axonal loss in multiple sclerosis lesions: magnetic resonance imaging insights into substrates of disability. *Ann Neurol*. 1999;46:747–754.
52. Slavin A, Ewing C, Liu J, Ichikawa M, Slavin J, Bernard CC. Induction of a multiple sclerosis-like disease in mice with an immunodominant epitope of myelin oligodendrocyte glycoprotein. *Autoimmunity*. 1998;28:109–120.
53. Wu Q, Butzkueven H, Gresle M, et al. MR diffusion changes correlate with ultra-structurally defined axonal degeneration in murine optic nerve. *Neuroimage*. 2007;37:1138–1147.
54. Albouz-Abo S, Wilson JC, Bernard CC, von Itzstein M. A conformational study of the human and rat encephalitogenic myelin oligodendrocyte glycoprotein peptides 35–55. *Eur J Biochem*. 1997;246:59–70.
55. Brown DA, Sawchenko PE. Time course and distribution of inflammatory and neurodegenerative events suggest structural bases for the pathogenesis of experimental autoimmune encephalomyelitis. *J Comp Neurol*. 2007;502:236–260.
56. Garthwaite G, Batchelor AM, Goodwin DA, et al. Pathological implications of iNOS expression in central white matter: an ex vivo study of optic nerves from rats with experimental allergic encephalomyelitis. *Eur J Neurosci*. 2005; 21:2127–2135.
57. Muller DM, Pender MP, Greer JM. A neuropathological analysis of experimental autoimmune encephalomyelitis with predominant brain stem and cerebellar involvement and differences between active and passive induction. *Acta Neuropathol*. 2000;100:174–182.
58. Tonra JR, Reister BS, Kolbeck R, et al. Comparison of the timing of acute blood-brain barrier breakdown to rabbit immunoglobulin G in the cerebellum and spinal cord of mice with experimental autoimmune encephalomyelitis. *J Comp Neurol*. 2001;430:131–144.
59. Thiessen JD, Zhang Y, Zhang H, et al. Quantitative MRI and ultrastructural examination of the cuprizone mouse model of demyelination. *NMR Biomed*. 2013;26(11):1562–1581.
60. LeBihan D, Breton E, Lallemand D, Grenier P, Cabanis E, Lavaljeantet M. MR imaging of intravoxel incoherent motions—applications to diffusion and perfusion in neurological disorders. *Radiology*. 1986;161(2):401–407.
61. Shindler KS, Revere K, Dutt M, Ying G-S, Chung DC. In vivo detection of experimental optic neuritis by pupillometry. *Exp Eye Res*. 2012;100:1–6.
62. Martin M, Reyes SD, Hiltner TD, et al. T2-weighted μMRI and evoked potential of the visual system measurements during the development of hypomyelinated transgenic mice. *Neurochem Res*. 2007;32:159–165.
63. Martin M, Hiltner TD, Wood JC, Fraser SE, Jacobs RE, Readhead C. Myelin deficiencies visualized in vivo: visually evoked potentials and T2-weighted magnetic resonance imaging of shiverer mutant and wild-type mice. *J Neurosci Res*. 2006;84:1716–1726.